fluids

MDPI

Article

Multi-Field Coupling and Data-Driven Based Optimization of Elliptical Nozzle Cooling

Fengli Yue [1,*], Yang Shao [1], Hongyun Sun [1], Jinsong Liu [2,3], Dayong Chen [2], Haitao Cui [3] and Yan Jia [1]

[1] Automotive and Transportation College, Shenyang Ligong University, Shenyang 110159, China; 15588358153@163.com (Y.S.); sunhy5006@163.com (H.S.); sylujy@126.com (Y.J.)
[2] Shi Changxu Materials Innovation Center, Institute of Metal Research, Chinese Academy of Sciences, Shenyang 110016, China; jsliu@imr.ac.cn (J.L.); dychen15b@imr.ac.cn (D.C.)
[3] Materials Science and Engineering College, Shenyang Ligong University, Shenyang 110159, China; cuihaitaoral@163.com
* Correspondence: flyue@163.com

Abstract

During the three-roll planetary rolling process, the cooling efficiency of conventional nozzle structures is insufficient, which can easily lead to copper adhesion on the roll surface, product quality degradation, and shortened roll lifespan, thereby limiting both the quality of copper tubes and overall production efficiency. To enhance the performance of the cooling system, this study proposes a novel elliptical nozzle structure and develops a multiphysics coupled model to reveal the effects of nozzle inclination angle and gas–liquid pressure ratio on cooling behavior. An independently constructed experimental platform was used to measure jet flow patterns and the surface temperature of alloy steel plates under various parameter conditions, thereby validating the accuracy and reliability of the numerical model. The results indicate that, under the same effective outlet area, the elliptical nozzle significantly increases jet exit velocity and overall cooling efficiency. To address the issues of high computational cost and low efficiency during optimization using finite element simulations, a high-accuracy surrogate model based on a Random Forest (RF) algorithm was introduced, and the geometric parameters of the nozzle were globally optimized using a Particle Swarm Optimization (PSO) algorithm. Ultimately, the combined RF-PSO strategy improved the average heat transfer coefficient by 55.57%, markedly enhancing the roll cooling performance and providing a solid theoretical basis and methodological reference for high-performance cooling system design and precision copper tube manufacturing.

Keywords: three-roll planetary rolling; machine learning; elliptical nozzle; spray cooling; heat transfer

check for updates

Academic Editor: Wei-Tao Wu

Received: 9 October 2025
Revised: 15 November 2025
Accepted: 28 November 2025
Published: 29 November 2025

Citation: Yue, F.; Shao, Y.; Sun, H.; Liu, J.; Chen, D.; Cui, H.; Jia, Y. Multi-Field Coupling and Data-Driven Based Optimization of Elliptical Nozzle Cooling. *Fluids* **2025**, *10*, 313. https://doi.org/10.3390/fluids10120313

Copyright: © 2025 by the authors. Licensee MDPI, Basel, Switzerland. This article is an open access article distributed under the terms and conditions of the Creative Commons Attribution (CC BY) license (https://creativecommons.org/licenses/by/4.0/).

1. Introduction

Three-roller planetary rolling, as an efficient metal plastic forming process, plays a crucial role in the fabrication of precision copper tubes. As illustrated in Figure 1a, the process employs the high-speed rotation of three sets of rollers, subjecting the metal billet simultaneously to radial, tangential, and axial forces. This enables continuous reduction in diameter and wall thickness as well as elongation of the tube billet. The technique not only significantly enhances forming efficiency and effectively reduces dimensional deviation but also improves the uniformity of microstructure and the overall performance of the material [1–4]. With the increasing demand from downstream industries for higher

quality and dimensional precision of copper tubes—particularly in the manufacturing of small-diameter tubes—three-roller planetary rolling has become the most critical stage, characterized by the largest deformation and the most significant influence on product quality. Studies have shown that this process effectively promotes microstructural refinement and mechanical property enhancement through dynamic recrystallization and grain refinement, thereby considerably improving the comprehensive performance of copper products [5]. As the core component of the three-roller planetary rolling process, the rollers directly interact with the tube surface, and their surface quality exerts a decisive impact on the geometric precision and microstructural properties of the rolled tubes [6]. Therefore, precise control of roller surface quality is of great importance for achieving grain refinement after rolling and for developing small-diameter, lightweight, high-performance copper tubes.

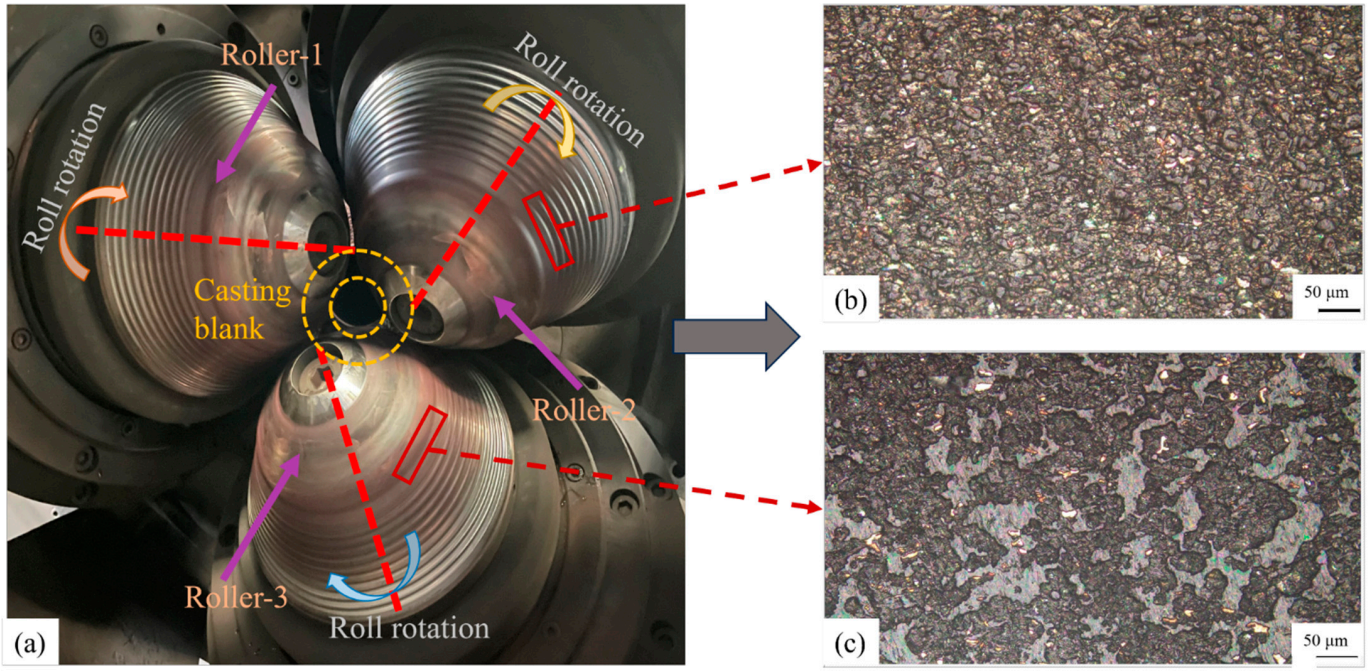


Figure 1. (**a**) Schematic diagram of three-roller planetary rolling, (**b**) concentrated deformation zone of the roller, and (**c**) copper adhesion phenomenon on the roller surface in the bite zone.

The three-roller planetary rolling process involves complex thermal–mechanical–fluid multi-physics coupling effects. During rolling, intense friction between the rollers and the billet, along with the plastic deformation heat of the copper billet, causes a rapid temperature rise at the contact interface [7–9]. If the cooling system lacks sufficient regulation capacity, uneven cooling will occur on the roller surface, leading to copper adhesion [10], as shown in Figure 1b,c. This phenomenon not only intensifies temperature fluctuations on the roller surface but also significantly accelerates thermal fatigue damage, thereby degrading the surface quality of the rollers [11,12]. Therefore, accurately understanding the temperature distribution and its evolution on the roller surface, as well as improving the cooling efficiency of the system, is of critical importance for enhancing roller surface quality and extending roller service life.

At present, roller cooling mainly relies on water-spray rings, with a typical water-cooling structure shown in Figure 2a. It can be seen that there are various combinations of the arrangement of the spray holes on the water-spray rings, but its essence is still to spray cooling liquid onto the surface of the rolls through several circular spray holes to achieve cooling. However, circular nozzles have obvious limitations in practical applications. Illyas

et al. [13] and Uddin et al. [14] reported that circular impinging jets provide high heat transfer intensity in the stagnation zone but are also characterized by a sharp stagnation peak and rapid radial decay. As a result, the heat transfer distribution on the surface becomes non-uniform, which reduces cooling efficiency, increases the temperature gradient on the roller surface, induces thermal stress, and ultimately shortens the service life of the rollers.

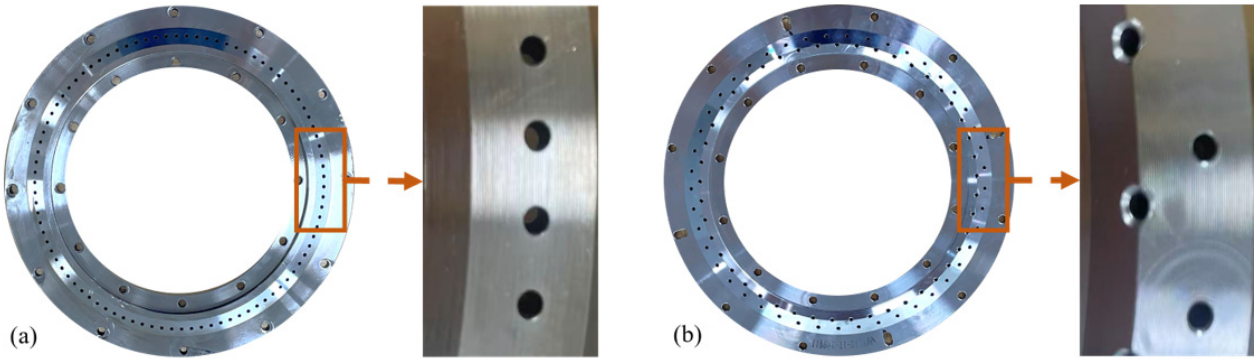


Figure 2. (**a**) Single-row spray-hole water ring and (**b**) multi-row spray-hole water ring.

Therefore, many researchers have shifted their attention to non-circular nozzles, such as elliptical nozzles and slot nozzles with aspect ratios greater than 10. Zuckerman et al. [15], Cademartori et al. [16], and Manca et al. [17] investigated slot jets and found that they can enhance cooling uniformity and increase the effective cooling area. Xu et al. [18] reported that elliptical nozzles provide higher average heat transfer under a given reference area, along with a wider effective cooling region. Joshi et al. [19] compared various nozzle geometries and found that elliptical nozzles can improve average heat transfer performance by up to 18%. These findings collectively demonstrate that elliptical nozzles offer significant advantages in improving cooling uniformity. However, it should be noted that the major and minor axes of an elliptical nozzle have a proportional relationship, and the rotation angle of the major axis around the nozzle center alters the directional distribution of heat transfer on the cooling surface, thereby exerting a significant influence on overall cooling uniformity [20,21]. Thus, accurately understanding the effect of the installation orientation of elliptical nozzles on cooling uniformity and cooling performance not only fills the gap in existing research but also provides direct theoretical guidance for setting cooling process parameters in practical rolling production.

To address the issues of excessive roll surface temperature and poor cooling uniformity of conventional circular nozzles in the three-roll planetary elongation process, this study proposes systematic innovations in both nozzle geometry and cooling strategy. A novel elliptical nozzle structure is developed and integrated with a gas–liquid enhanced cooling approach, in which nitrogen is introduced to increase the kinetic energy of the coolant jet, thereby improving heat transfer performance and flow field distribution. A coupled fluid–solid–thermal finite element model is then established to quantitatively investigate the effects of gas–liquid pressure ratio and the rotation angle of the elliptical nozzle major axis on the evolution of the temperature field and cooling uniformity, revealing the underlying influence mechanisms of key parameters on cooling behavior. Furthermore, a machine learning–based surrogate model combined with an intelligent optimization algorithm is employed to achieve multi-objective optimization of nozzle parameters, enabling coordinated enhancement of cooling performance and structural design. The findings provide an effective technical route and theoretical basis for structural upgrading and intelligent optimization of roll cooling systems in three-roll planetary elongation mills.

2. Design and Simulation of a Novel Water-Spray Ring Structure

2.1. Structural Design

Elliptical nozzles have demonstrated significant advantages in enhancing cooling efficiency and improving cooling uniformity. Building upon the findings of Joshi [19] and Schuller [22], this study designs a novel water-spray ring equipped with elliptical nozzles, as shown in Figure 3. Based on the classical double-row hole arrangement, the spray ring maintains injection angles of horizontal and 18° outward to ensure a wide cooling coverage area; the nozzles are evenly distributed along the circumference, thereby achieving uniform cooling of the roller surface. Compared with traditional circular nozzles, the nozzle structure in this study introduces innovative improvements by adopting a bolted interface, which allows multi-angle rotation and replacement with different specifications. Specifically, the nozzle is designed in a bolt style that matches the spray ring, with an elliptical orifice at the head, a cylindrical flow channel inside, and a smooth transition structure along the minor axis to reduce flow losses. In addition, triangular diffusion grooves are arranged along the major axis at the nozzle head to enhance the diffusion and coverage of the coolant, thereby further improving cooling performance.

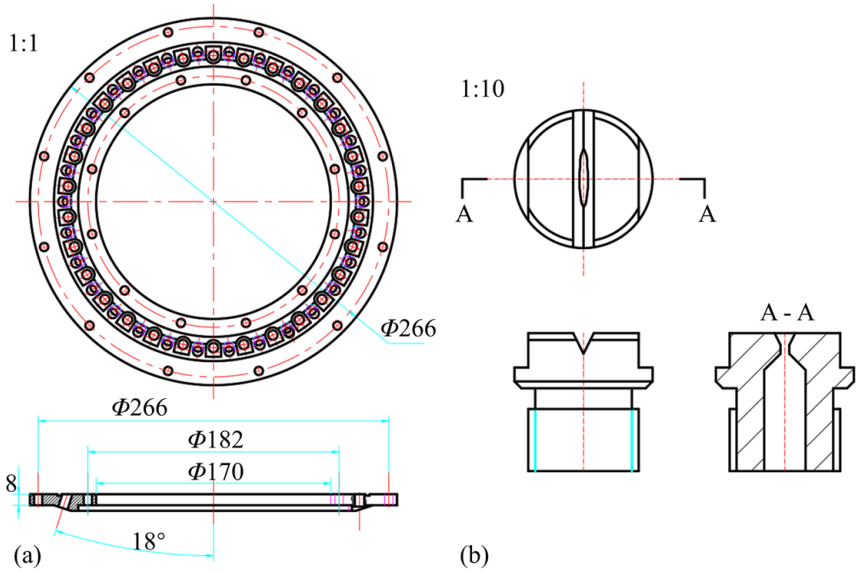


Figure 3. (**a**) Novel water-spray ring structure and (**b**) novel nozzle structure.

2.2. Control Equation

Based on multi-physics coupling, computational analysis requires the fluid domain to satisfy the continuity equation, momentum conservation equation, and energy conservation equation [23,24]. Meanwhile, to simulate the gas–liquid interaction inside the nozzle, the Volume of Fluid (VOF) method is employed.

(1) VOF method

The VOF model is used to track the interface between multiple immiscible fluids, so a single computational cell may simultaneously contain more than one fluid. Since the governing physical equations require each cell to have a unique density and viscosity, the equivalent physical properties of the cell are calculated using a volume-fraction weighted averaging method [25].

$$\rho_E = \alpha \cdot \rho_1 + (1 - \alpha)\rho_2 \quad (1)$$

$$\mu_E = \alpha \cdot \mu_1 + (1 - \alpha)\mu_2 \quad (2)$$

where ρ_E is the equivalent density of the current computational cell, μ_E is the equivalent viscosity of the current cell, α is the volume fraction of the fluid in the cell, and ρ_1, ρ_2, μ_1 and μ_2 are the densities and viscosities of fluid 1 and fluid 2, respectively.

(2) Continuity equation

$$\frac{\partial \rho_E}{\partial t} + \nabla \cdot (\rho_E u) = 0 \tag{3}$$

where u is the continuous phase velocity, and t is time.

(3) Momentum conservation equation

$$\begin{cases} \dfrac{\partial(\rho_E u_x)}{\partial t} + \nabla \cdot (\rho_E u_x \mathbf{U}) = \nabla \cdot (\mu_E \nabla u_x) - \dfrac{\partial p}{\partial x} + F_x \\ \dfrac{\partial(\rho_E u_y)}{\partial t} + \nabla \cdot (\rho_E u_y \mathbf{U}) = \nabla \cdot (\mu_E \nabla u_y) - \dfrac{\partial p}{\partial y} + F_y \\ \dfrac{\partial(\rho_E u_z)}{\partial t} + \nabla \cdot (\rho_E u_z \mathbf{U}) = \nabla \cdot (\mu_E \nabla u_z) - \dfrac{\partial p}{\partial z} + F_z \end{cases} \tag{4}$$

where $\mathbf{U}$ is the velocity vector, and F_x, F_y, F_z is the components of the external force term in all directions.

(4) Energy conservation equation

$$\frac{\partial\left(\rho_E E_f\right)}{\partial t} + \nabla \cdot \left(\rho_E u E_f\right) = \nabla \cdot \left(k_f \nabla T_f\right) + \nabla \cdot (\tau \cdot u) \tag{5}$$

where E_f is the total energy of the fluid, k_f is the thermal conductivity of the fluid, and T_f is the temperature of the fluid.

(5) Turbulence model

$$\frac{\partial(\rho_E k)}{\partial t} + \nabla \cdot (\rho_E k u) = \nabla \cdot \left[\left(\mu_E + \frac{\mu_t}{\sigma_k}\right)\nabla k\right] + G_k - \rho_E \varepsilon \tag{6}$$

$$\frac{\partial(\rho_E \varepsilon)}{\partial t} + \nabla \cdot (\rho_E \varepsilon u) = \nabla \cdot \left[\left(\mu_E + \frac{\mu_t}{\sigma_\varepsilon}\right)\nabla \varepsilon\right] + C_1 f_1 \frac{\varepsilon}{k} G_k - C_2 f_2 \rho_E \frac{\varepsilon^2}{k} \tag{7}$$

where the constant C_1 is 1.44 and C_2 is 1.92, which is the turbulence generation term.

2.3. Boundary Conditions

2.3.1. Inlet and Outlet

To improve the accuracy of the finite element model and ensure consistency with the actual operating conditions, the boundary conditions were defined strictly based on the experimental setup. Both the inlet and outlet were specified as pressure boundary conditions to represent the real pressure distribution during the cooling process. Inlet 1 was assigned as the cooling-water inlet with a temperature of 300 K, while Inlet 2 was defined as the cooling-water or nitrogen-gas inlet, also maintained at 300 K to remain consistent with the experimental environment. In addition, to accurately capture the interaction at the gas–liquid interface, the surface-tension model was activated in the VOF framework, and the water–air interfacial tension coefficient was set to 0.0728 N/m. This configuration allows the two-phase flow behavior and interface deformation to be represented more realistically.

2.3.2. Cooling Plate

During the rolling process, the temperature rise in the rollers is primarily influenced by heat conduction from the copper tube and frictional heat, while the heat exchange through radiation with the surrounding environment is relatively small. Therefore, in

this study, the radiation heat transfer is neglected to simplify the model. As a result, the heat transfer of the cooling plate is mainly considered as convective heat exchange with the coolant:

$$-k\frac{\partial T}{\partial n}\bigg|_{\Gamma} = q_{\text{conv}} + q_{\text{sens}} + q_{\text{evap}} \tag{8}$$

where q_{conv} mainly considers convective heat transfer between cooling liquid and plate, q_{sens} mainly considers temperature rise during coolant heat exchange, and q_{evap} mainly considers evaporation latent heat absorption during coolant heat exchange [26].

$$\begin{cases} q_{\text{conv}} = h\left(T_{\text{s}} - T_{\text{liq}}\right) \\ q_{\text{sens}} = \dot{m}_{\text{evap}}\, c_p\left(T_{boil} - T_{\text{liq}}\right) \\ q_{\text{evap}} = \dot{m}_{\text{evap}}\, L \end{cases} \tag{9}$$

where T_s is the cooling plate temperature, T_{liq} is the initial temperature of cooling liquid, T_{boil} is the boiling temperature of cooling liquid, usually 373.15 K, and L is the latent heat of vaporization of cooling liquid.

2.3.3. Evaporation Boundary

During the cooling process, when the low-temperature cooling liquid comes into instant contact with the high-temperature surface of the cooling plate, partial evaporation occurs. In this process, not only sensible heat transfer of the liquid phase takes place, but also significant latent heat exchange. To improve the accuracy of the finite element model, the evaporation mass flux in Equation (9) is mainly determined by the following formula [27]:

$$\dot{m}_{\text{evap}} = k_c \cdot A_m \cdot \rho_l \cdot (Y_{\text{sat}} - Y_\infty) \tag{10}$$

where k_c is the mass transfer coefficient, which is related to Reynolds number and Schmidt number, A_m is evaporation area, and Y_{sat} is saturation mass fraction.

2.3.4. Liquid Film Flow

When cooling liquid is sprayed onto the surface of the cooling plate, it does not completely evaporate. A portion of the water remains in liquid form and flows away without full vaporization, due to reasons such as insufficient heat absorption, excessive flow velocity, vapor film effects, or inadequate contact.

$$u = \frac{\rho \cdot g \cdot \delta^2}{3 \cdot \mu_E} \tag{11}$$

$$\frac{d}{dt}(\rho_E \cdot \delta) + \nabla \cdot \left(\rho_E \cdot \delta \cdot \vec{u}\right) = \dot{m}_{\text{in}} - \dot{m}_{\text{evap}} \tag{12}$$

where δ is the thickness of the liquid film and $\dot{m}_{\text{in}}$ is the quality source item for liquid film supplementation.

2.4. Finite Element Model

Taking the circular nozzle as an example, the geometric model of the spray ring is shown in Figure 4a. It contains two relatively independent internal flow domains that enable the simultaneous supply of two cooling media. In addition, several arrays of circular holes connect the two flow domains, allowing the cooling media to circulate between them. During the construction of the finite element model, the spray ring structure was partially simplified to reduce computational cost. To improve mesh

quality and numerical stability, the annular structure was simplified to a rectangular form in the model, and its fluid domain was extracted to build the internal flow model, as shown in Figure 4b.

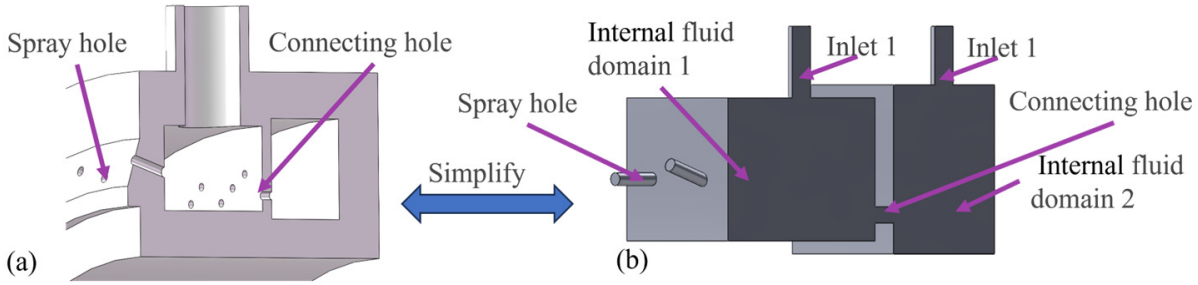


Figure 4. (**a**) Geometric model of the water spray ring and (**b**) Simplified model of the water spray ring.

A finite element model was constructed using the Fluent platform based on the actual physical configuration. A cooling plate model was positioned H in front of the nozzle, and a geometric fluid domain was created to enclose it. The final computational model is shown in Figure 5a. Two key parameters were selected for the simulation: the gas–liquid pressure ratio (α) and the inclination angle (β) of the elliptical nozzle, as illustrated in Figure 5b. The inclination angle β is defined as the angle between the major axis of the elliptical nozzle and the vertical direction. In the simulation, Fluid Domain 1 was completely filled with cooling liquid, while Fluid Domain 2 was filled with either cooling liquid or nitrogen depending on the operating conditions. To investigate different jet characteristics, the inclination angle of the elliptical nozzle was varied by adjusting the nozzle structure and orientation.

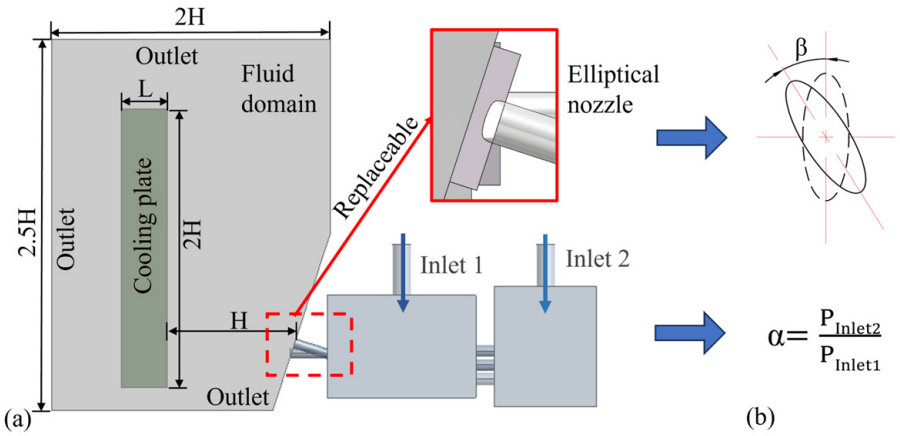


Figure 5. (**a**) Finite element model, and (**b**) simulation parameters (gas–liquid pressure ratio α: inlet pressure of cooling media at Inlet 1 and Inlet 2; inclination angle β: rotation angle of the major axis of the elliptical nozzle relative to the vertical direction).

In the numerical simulation, the VOF model was employed to quantitatively analyze the cooling liquid velocity at the nozzle outlet and the cooling performance of the cooling plate under different structural parameters of the nozzle. The cooling plate material was 3Cr2W8V alloy steel, and the cooling medium was a mixture of water and emulsion. The addition of the emulsion alters the thermophysical properties of the coolant and forms an oil film on the roller surface, thereby affecting the cooling performance [28]. In this study, the emulsion concentration was set to 5%. Table 1 lists the thermophysical properties of the materials and the simulation parameters, which remained constant throughout the analysis [29].

Table 1. Simulation process parameters.

Characteristic Parameter	Cooling Plate	Cooling Liquid
Density kg/m^3	7800	989.65
Specific Heat J/(kg·K)	460	4089.6
Thermal Conductivity W/(m·K)	26.14	0.5765
Dynamic Viscosity Pa·s		0.00113

The computational time required for the simulation increases proportionally with the number of mesh elements. Although reducing the mesh density can improve computational efficiency, it inevitably decreases the calculation accuracy. Therefore, it is essential to achieve a reasonable balance between accuracy and efficiency. To determine an appropriate mesh density, this study compared the average outlet velocity of the nozzle under different mesh quantities, as summarized in Table 2. The results show that when the mesh count ranges from 9.42 to 14.62 million, the average outlet velocity remains nearly unchanged. Hence, a mesh density of approximately 9.42 million elements was finally selected for model construction, as illustrated in Figure 6a,b.

Table 2. Mesh independence.

Mesh Quantity (W)	502	672	942	1142	1462
Average flow velocity (m/s)	16.69	17	17.25	17.256	17.24

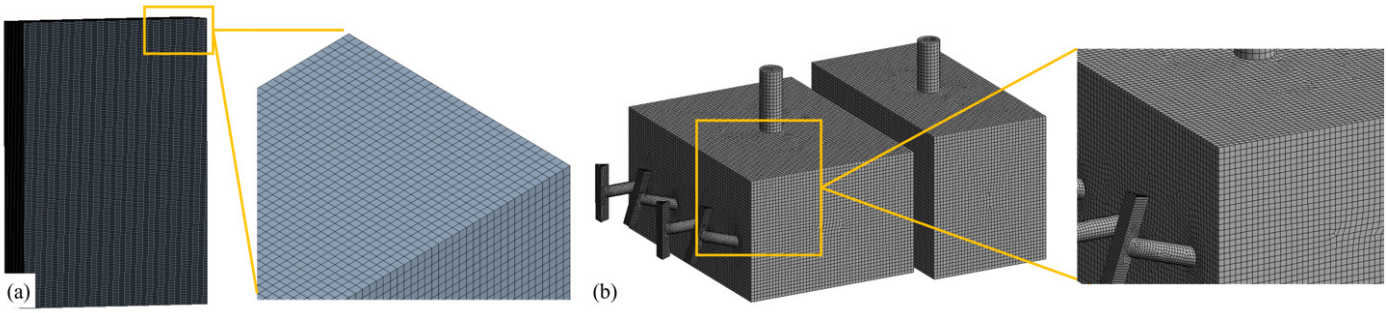


Figure 6. (**a**) Cooling plate mesh and (**b**) nozzle grid model.

3. Analysis of Simulation Results and Experimental Verification

3.1. Simulation Results

Considering the computational time and cost, a fixed simulation time step was adopted to analyze the velocity distribution of cooling liquid at the nozzle outlet under different nozzle inclination angles and gas–liquid pressure ratios, as summarized in Table 3. For each value of α, a circular nozzle was included as a reference for comparison.

Table 3. All simulated process parameters.

	Circular Nozzle	Elliptical Nozzle	
	Gas–Liquid Pressure Ratio (α)	Gas–Liquid Pressure Ratio (α)	Inclination Angle (β)
Value	0	0	0°
	1	1	30°
	2	2	45°
	3	3	60°
	4	4	90°
	5	5	

As shown in Figure 7, when the cooling liquid flows from the inner cavity into the nozzle channel, the effective flow area decreases, resulting in a significant increase in velocity. For the circular nozzle, the sudden contraction from the chamber to the narrow outlet causes pronounced local separation and contraction effects, leading to considerable energy loss [30]. In contrast, the elliptical nozzle has a larger diameter and lower flow resistance. Its gradual transition along the minor axis allows a smoother contraction process and weaker separation effects. Meanwhile, the major axis of the elliptical nozzle matches the inlet channel diameter, minimizing additional contraction and maintaining a more uniform velocity distribution. Moreover, under the influence of surface tension, the cooling liquid expands further along the major axis at the outlet [31]. Therefore, the elliptical nozzle achieves a higher outlet velocity than the circular one under identical operating conditions.

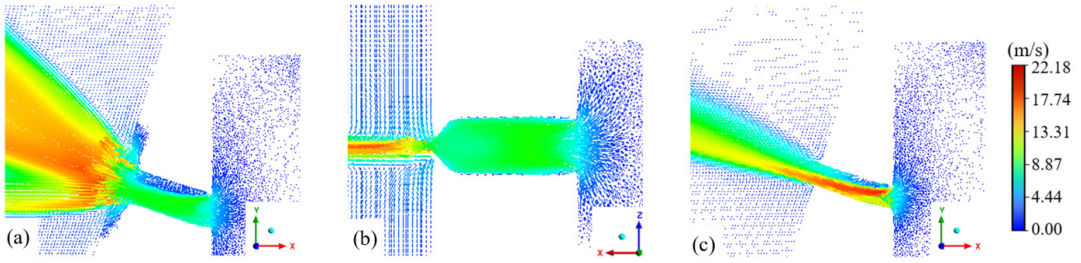


Figure 7. Outlet velocity distribution on the three characteristic planes at $\alpha = 2$: (**a**) major-axis plane of the elliptical nozzle, (**b**) minor-axis plane of the elliptical nozzle, and (**c**) diameter plane of the circular nozzle.

The temperature contour shown in Figure 8 represents the surface temperature distribution on the front face of the cooling plate located downstream of the nozzle outlet and directly facing the nozzle. The temperature field corresponds to the entire exposed surface. It can be observed that the cooling region formed by the circular nozzle exhibits a typical axisymmetric circular pattern that gradually decays and diffuses radially. In contrast, the cooling distribution of the elliptical nozzle does not present an elliptical cooling band consistent with its geometry, but instead displays multiple local cooling centers along the major axis. This phenomenon mainly arises from the non-axisymmetric characteristics of the elliptical jet: in the major-axis direction, large-scale vortex structures are more easily induced, and when these vortices impinge on the wall surface, they locally concentrate momentum and turbulent kinetic energy, leading to the formation of several enhanced heat transfer regions [32]. However, from an overall perspective, the jet coverage of the elliptical nozzle is significantly larger than that of the circular nozzle, with particularly improved cooling performance in the edge regions. Therefore, although elliptical nozzles generate multiple local cooling centers due to flow instability and vortex effects, these centers are continuously distributed with relatively small overall temperature fluctuations, resulting in superior overall cooling performance and uniformity compared to circular nozzles.

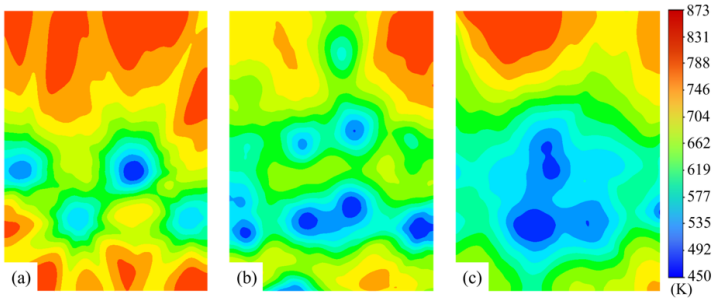


Figure 8. Cloud map of the surface temperature distribution of the cooling plate before the nozzle: (**a**) circular nozzle, (**b**) elliptical nozzle at $\alpha = 0°$ and (**c**) elliptical nozzle at $\alpha = 90°$.

3.2. Experimental Results

To validate the simulation results, an experimental setup was established, as shown in Figure 9a. The setup mainly consists of a high-temperature plate, a spray regulation system, and a data acquisition system. The high-temperature plate is made of a high-temperature alloy steel plate heated externally, serving as the target for the cooling study. The spray regulation system includes components such as the nozzle, water tank, pressure vessel, and pressure gauges, and utilizes nitrogen pressure to adjust the jet velocity of the cooling liquid. The data acquisition system comprises an infrared thermometer, a data control board, a high-speed camera, and a computer. The infrared thermometer is used to record the surface temperature after cooling, with a spectral range of 0.7–2.6 μm, an adjustable emissivity range of 5–120%, and a measurement accuracy higher than 0.5%. The high-speed camera is employed to observe the jet morphology, as shown in Figure 9b. During the experiment, a PLC program controls the opening and closing of solenoid valves to achieve precise control of jet pressure and duration, as illustrated in Figure 9c.

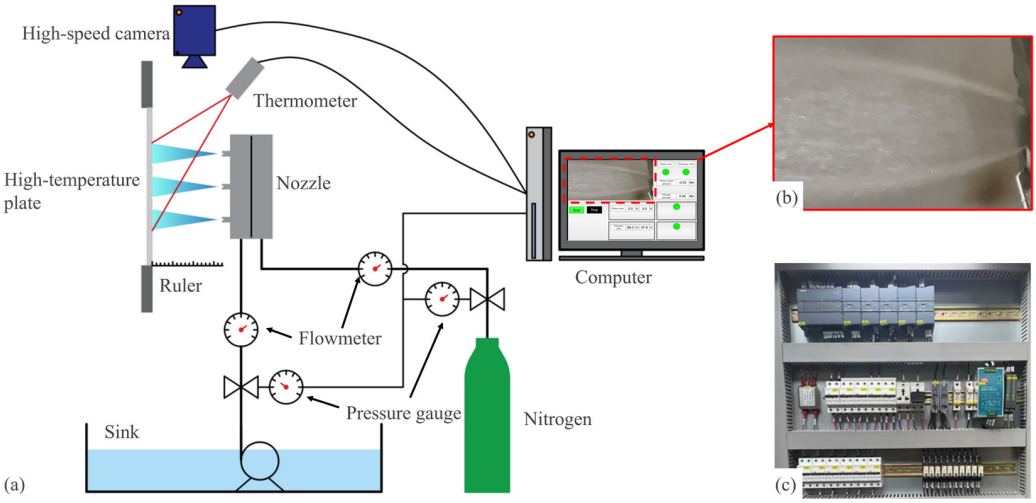


Figure 9. (**a**) Experimental setup, (**b**) water flow state of the elliptical nozzle and (**c**) control system of the experimental setup.

Using the experimental setup shown in Figure 9, experiments were conducted on the elliptical nozzle at nozzle angles and the circular nozzle under gas–liquid ratios of 0 and 2. During the experiments, after cooling for 10 s, the surface temperature of the cooling plate and the spray status of the coolant were recorded. Within the study area, 500 characteristic points were evenly selected for temperature measurement and statistical analysis. Each experiment was repeated three times under the same operating conditions, and the average value was taken as the final data. During measurement, the accuracy of the infrared thermometer and system errors were considered, and data uncertainty was quantified using the standard deviation, with a maximum error of less than ±0.8 °C. Subsequently, the heat transfer coefficient on the cooling plate surface under different nozzle parameters was calculated according to Equation (13), and the results are shown in Table 4.

$$h = -\frac{\rho c_p V}{At} \cdot \ln\left(\frac{T(t) - T_\infty}{T_i - T_\infty}\right) \tag{13}$$

where T_i is the initial roller surface temperature, $T(t)$ is the average roller temperature after cooling, T_∞ is the cooling liquid temperature, C_p is the specific heat capacity at constant pressure of the 3Cr2W8V alloy steel, V is the volume of the study area, and A is the surface area of the study area.

Table 4. Experimental measurement of temperature.

Nozzle Inclination Angle		Circular	β = 0°	β = 30°	β = 45°	β = 60°	β = 90°
Heat transfer coefficient ($W/m^2 \cdot K$)	α = 0	4922.83	8428.82	9235.85	9906.53	9338.23	8088.81
	α = 2	9830.91	10,396.38	12,239.97	12,887.13	13,362.75	10,293.47

As shown in Table 4, under the same gas–liquid ratio conditions, the heat transfer coefficient on the cooling plate surface first increases and then decreases with changes in the elliptical nozzle inclination angle. This phenomenon mainly arises from the anisotropic characteristics of elliptical nozzle jets: along the major axis, the velocity distribution is smoother with a wider coverage, whereas along the minor axis, the velocity gradient is steeper and the jet diffusion is more concentrated. When the nozzle inclination angle changes, both the coverage area and the superposition effects between multiple jets are adjusted accordingly, leading to variations in the heat transfer coefficient on the cooling plate surface.

In addition, Table 4 also shows that with an increasing gas–liquid ratio, the heat transfer coefficient on the cooling plate surface is significantly enhanced. This is primarily because a higher gas–liquid ratio results in an increased nozzle outlet velocity, which intensifies wall turbulence and ultimately improves heat transfer performance.

Figure 10 presents the coolant jet states obtained from numerical simulations and experiments. It is evident that the experimental results and simulations exhibit a high degree of consistency in the flow characteristics of the cooling liquid discharged from the nozzle. Both the overall flow field distribution and the decay of velocity from the nozzle outlet to the downstream region in the simulations closely match the experimental observations. Furthermore, good similarity is observed in terms of the diffusion range and flow patterns at the jet periphery. These results demonstrate that the developed numerical model can accurately capture the main features of the nozzle flow field, thereby confirming the reliability and effectiveness of the simulation method for predicting nozzle flow behavior.

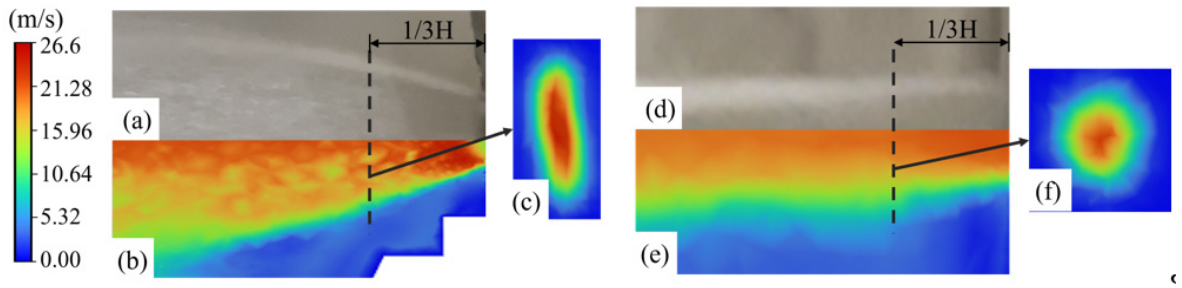


Figure 10. Coolant medium ejection state (**a**) experimental results of elliptical nozzle (**b**) simulation results of elliptical nozzle (**c**) simulation results of the cross-section at the front 1/3 H of the elliptical nozzle (**d**) experimental results of circular nozzle, (**e**) simulation results of circular nozzle, and (**f**) simulation results of the cross-section at the front 1/3 H of circular nozzle.

The heat transfer coefficients under the same parameter conditions, obtained from both experimental measurements and numerical simulations, are shown in Figure 11. It can be seen that the two exhibit the same trend. By calculating the relative error using Equation (14), the results indicate that the maximum and minimum errors between the simulation and experimental results are 4.73% and 0.45%, respectively. During the numerical simulation, since the flow rate and velocity of each individual nozzle are consistent with

the experimental conditions, the local cooling behavior shows a quantifiable agreement, effectively reflecting the local cooling patterns observed in the experiments.

$$\delta = \frac{\left|X_{sim} - X_{\exp}\right|}{X_{\exp}} \times 100\% \quad (14)$$

where X_{sim} is the heat transfer coefficient obtained through simulation calculation, $X_{\exp}$ is the heat transfer coefficient obtained through experimental calculation.

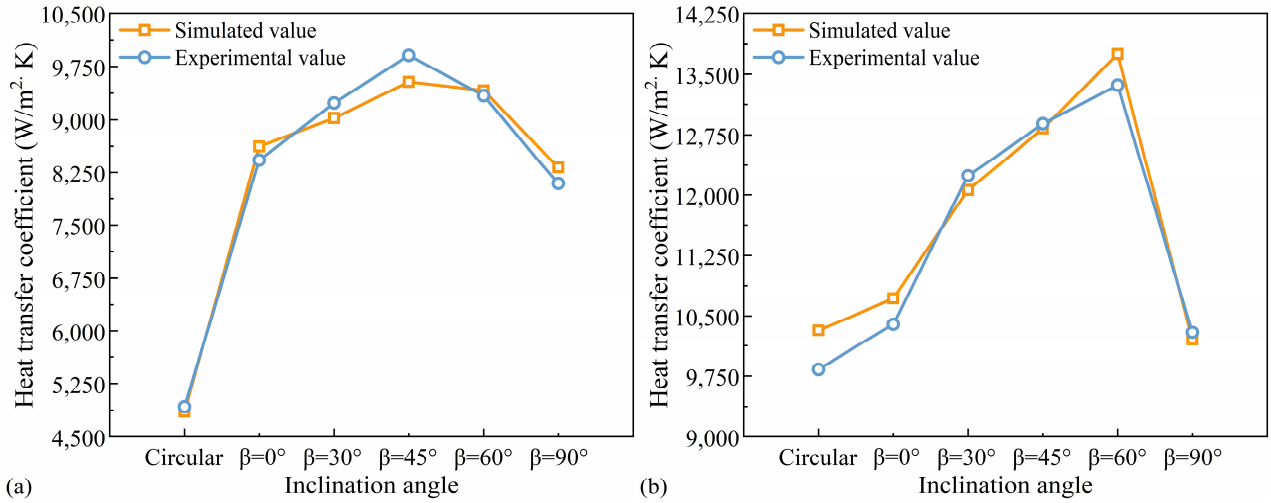


Figure 11. Comparison of the heat transfer coefficients of the cooling plate surface at each inclination Angle of the circular nozzle and the elliptical nozzle at (**a**) β = 0 and (**b**) β = 2.

3.3. Comparison Between Round Holes and Elliptical Nozzles

From the velocity contour in Figure 10, it is evident that under the same gas–liquid pressure ratio, the elliptical nozzle produces a larger high-velocity region and a more uniform jet compared with the circular nozzle, resulting in a higher average outlet velocity. This difference mainly arises from their geometric structures: the circular orifice imposes stronger flow confinement, leading to jet contraction, reduced effective flow area, and greater energy loss, whereas the elliptical nozzle suffers less contraction and therefore has a higher flow coefficient and outlet velocity [33].

Combined with the temperature distribution from experiments and simulations, the elliptical nozzle also demonstrates superior cooling performance under identical conditions, providing a larger effective cooling area, better edge-region heat transfer, and more uniform temperature reduction. In summary, considering both jet velocity and cooling effectiveness, the elliptical nozzle outperforms the circular nozzle, and subsequent research will focus on its parametric optimization.

4. Parameter Discussion

4.1. The Influence on Flow Velocity

A total of 100 monitoring points were evenly selected on the end face of each nozzle hole, and the velocity distribution was recorded after the flow field stabilized to calculate the average outlet velocity, as shown in Figure 12a,b. The results indicate that the average outlet velocity shows little variation with changes in the inclination angle of the elliptical nozzle. This is mainly because the nozzle inlets all have the same circular tube structure, resulting in consistent inlet flow conditions, so changes in the inclination angle have a limited effect on the overall flow velocity.

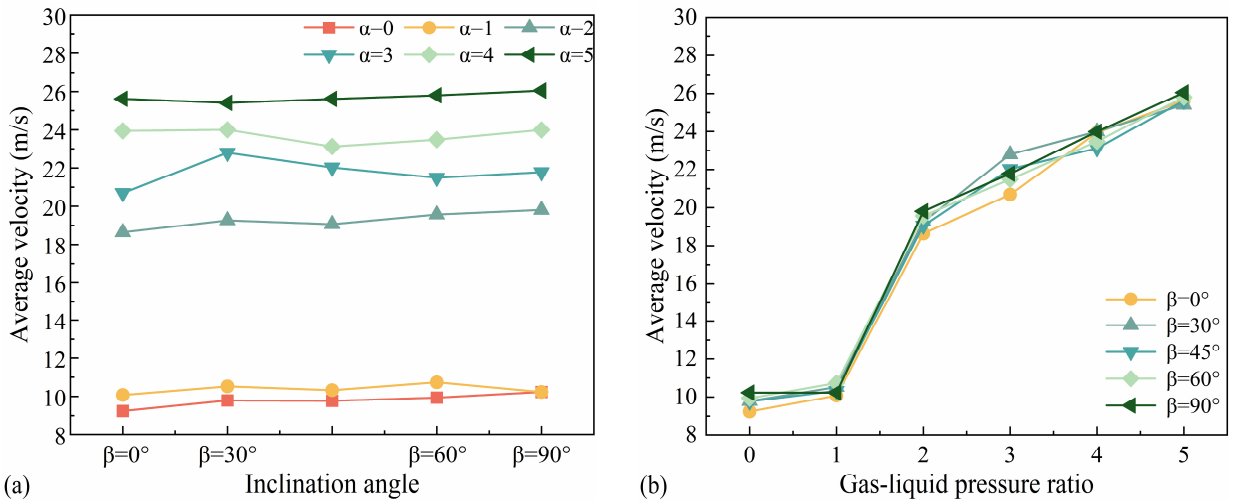


Figure 12. Variation curves of the elliptical nozzle average velocity with (**a**) nozzle inclination angle and (**b**) gas–liquid pressure ratio.

Further comparison of the average velocity under different gas–liquid pressure ratios shows that when the pressure ratio is 0 or 1, the outlet velocity difference is small; however, when the pressure ratio exceeds 2, the velocity increases significantly and continues to rise with the increasing pressure ratio. This is because the nozzle cavity is already filled with water before nitrogen is supplied, and when the gas–liquid inlet pressures are equal, nitrogen cannot generate an effective pressure difference. It only forms bubbles within the water, altering the local flow structure [34]. Therefore, under low pressure ratio conditions, the driving effect of nitrogen is limited, resulting in a weak impact on the flow velocity, which is why the velocity difference between pressure ratios 0 and 1 is insignificant.

4.2. The Influence on Momentum Flux

During the cooling process, a higher momentum flux of the coolant leads to a stronger jet impingement, more effective disruption of the boundary layer, and enhanced local convective heat transfer. Therefore, momentum flux serves as an important indicator for evaluating cooling performance and optimizing nozzle design. In this study, the momentum flux at the nozzle exit was calculated using Equation (14):

$$M = \iint_A \rho u_n^2 dA \tag{15}$$

where M is the total momentum flux, u_n is the component of the velocity in the normal direction of the exit, and A is the cross-sectional area of the exit.

Figure 13 shows the variation in momentum flux with the inclination angle of the elliptical nozzle and the gas–liquid pressure ratio. When β = 45°, the momentum flux is noticeably lower than at other angles, mainly due to the uneven velocity distribution over the elliptical cross-section and its projection relative to the jet direction. In contrast, at β = 0° and 90°, the velocity components remain aligned with the principal axis, leading to smaller disturbances and weaker changes in momentum flux. Increasing the gas–liquid pressure ratio significantly raises the momentum flux, consistent with its approximate dependence on the square of the jet velocity. A higher gas–liquid pressure ratio further strengthens momentum exchange, demonstrating the coupled enhancement effect of nozzle geometry and gas–liquid interaction [35,36].

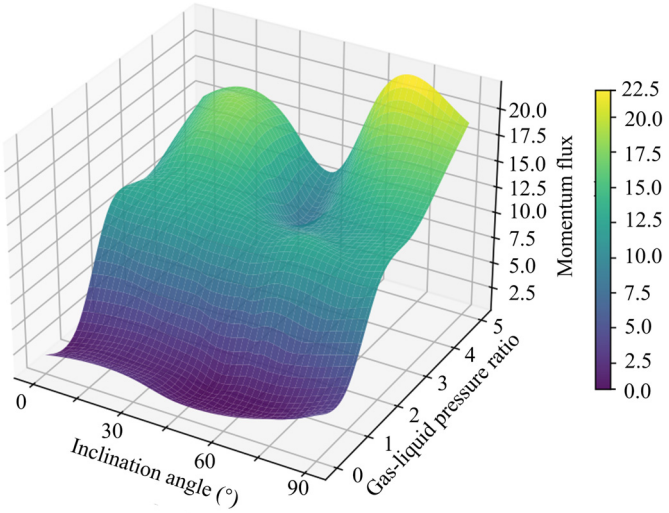


Figure 13. The response graph of the momentum flux at the outlet of an elliptical nozzle to the nozzle inclination Angle and the gas–liquid pressure ratio.

4.3. The Influence on the Surface Temperature of the Cooling Plate

The temperatures at 500 monitoring points on the surface of the cooled plate were statistically analyzed and averaged to generate the temperature distribution shown in Figure 14. Under the same gas–liquid pressure ratio, different nozzle rotation angles produce distinct effects on the plate temperature distribution: at 0°, the nozzle coverage is wide but cooling is insufficient in the gap regions, resulting in noticeable local hotspots; at 90°, the horizontal arrangement of the nozzle causes overlap of the cooled areas, yielding the highest average plate temperature [37].

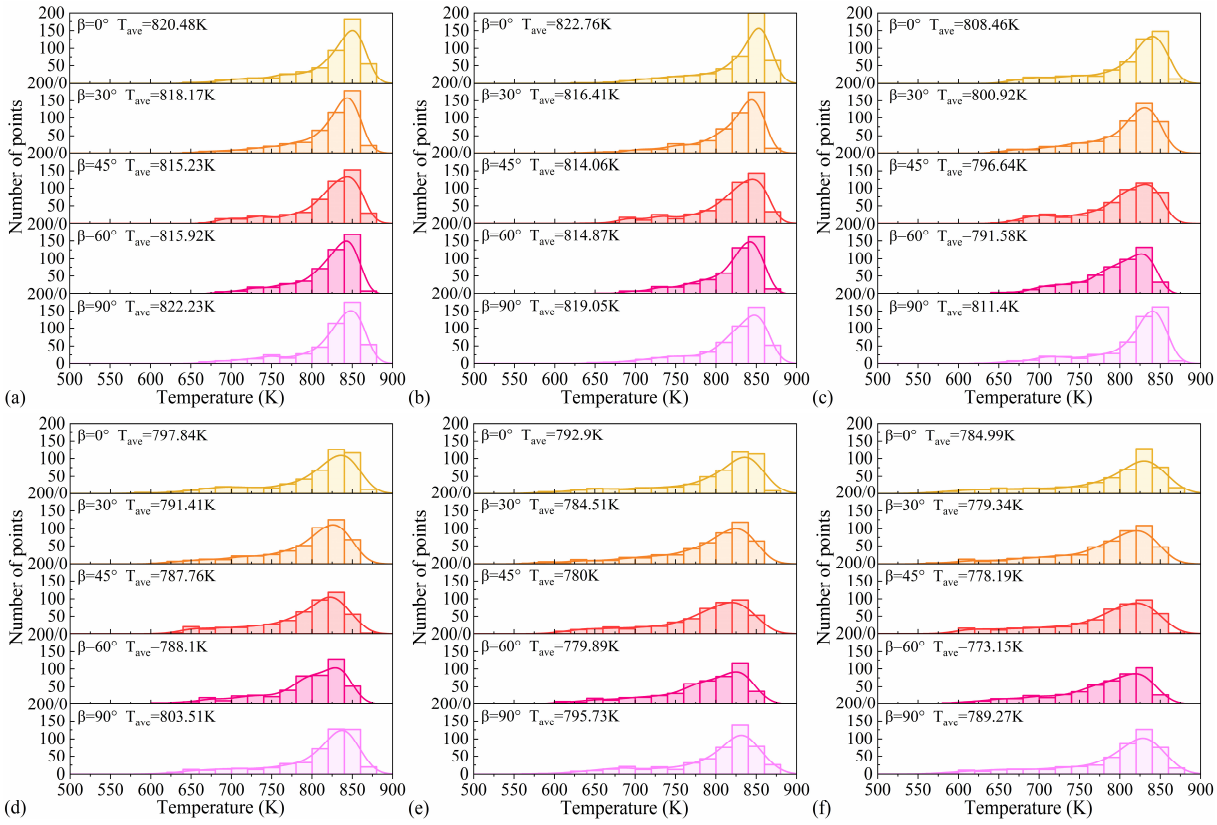


Figure 14. Variation curves of average cooling plate surface temperature with nozzle inclination angle at (**a**) $\alpha = 0$, (**b**) $\alpha = 1$, (**c**) $\alpha = 2$, (**d**) $\alpha = 3$, (**e**) $\alpha = 4$, and (**f**) $\alpha = 5$.

As the gas–liquid pressure ratio increases, the average plate temperature decreases, indicating enhanced cooling efficiency. When the pressure ratio exceeds 2, the temperature peaks are reduced and the plateau regions extend, showing that a higher pressure ratio not only strengthens the cooling effect but also improves the uniformity of the plate temperature, particularly at the edges. Further increasing the pressure ratio continues to improve cooling performance, but the rate of improvement gradually diminishes.

4.4. The Influence on the Heat Flux on the Surface of the Cooling Plate

The distribution of heat flux on the cooled plate directly affects the overall cooling efficiency. To investigate the influence of the elliptical nozzle inclination angle on the heat flux distribution, sampling was conducted along the paths shown in Figure 15a: Line 1 corresponds to the centerline between nozzles, while Line 2 and Line 3 correspond to the central axes of the nozzle cooling regions. Along each sampling line, 120 temperature points were evenly selected, and the heat flux distribution curves were plotted accordingly Figure 15b–d.

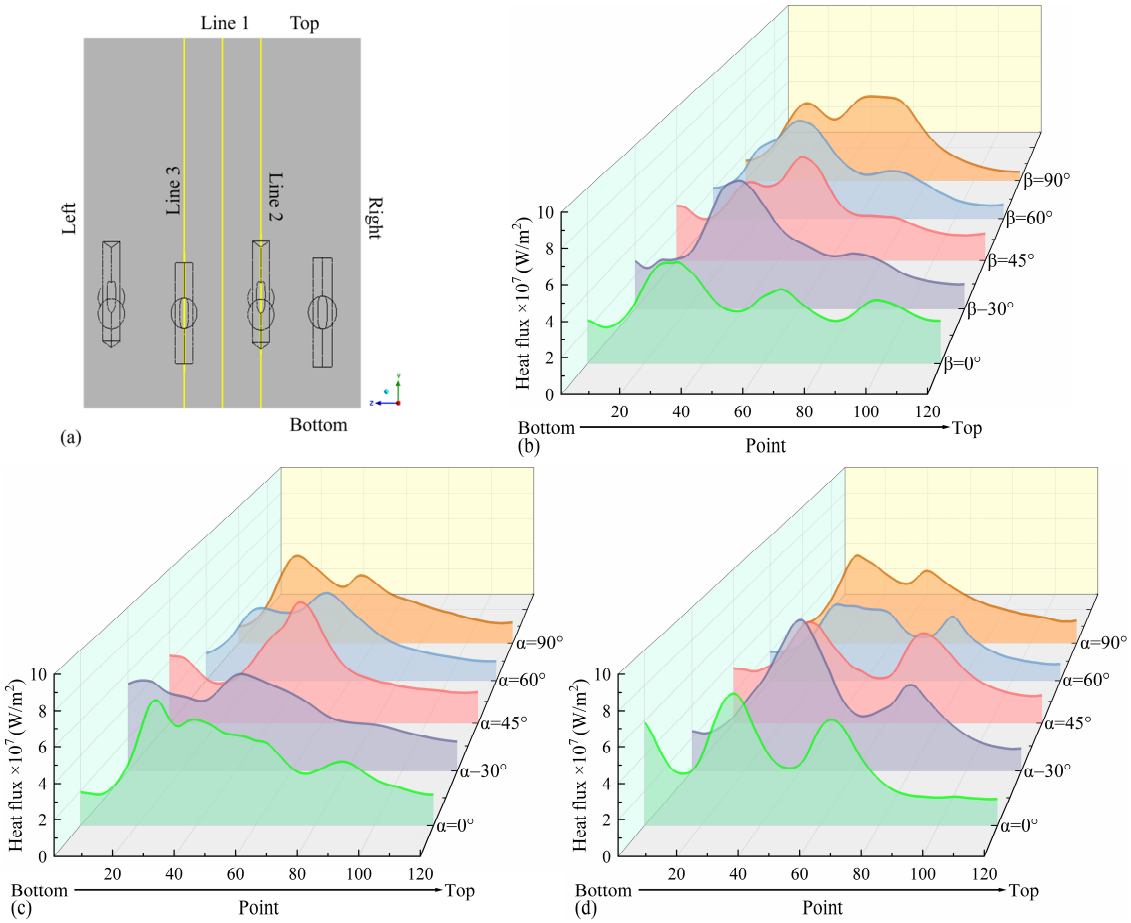


Figure 15. (**a**) Division of the cooling plate research area, (**b**) heat flux distribution map of Line 1, (**c**) heat flux distribution map of Line 2 and (**d**) heat flux distribution map of Line 3.

The results indicate that the elliptical nozzle produces a superposition effect in the central region, generating distinct cooling peaks, but the overall heat flux uniformity is poor. As the inclination angle increases from 0° to 90°, the uniformity of the heat flux distribution is significantly improved, although the effective cooling area gradually decreases. Specifically, at $\beta = 0°$, the peaks are concentrated at the nozzle projection positions and decay rapidly afterward, which is unfavorable for uniform cooling. As the

inclination angle increases, the superposition effect is enhanced, the decay between peaks is reduced, and the uniformity of the cooling distribution is improved [38,39].

In summary, the inclination angle of the elliptical nozzle has a nonlinear effect on cooling performance, with an optimal angle at which the best cooling effect can be achieved. Regarding the gas–liquid pressure ratio, considering production costs and field operating conditions, there also exists an optimal range. As the gas–liquid pressure ratio increases further, although the cooling performance tends to decline, the rate of decrease gradually slows. Therefore, an economically optimal pressure ratio can be determined that satisfies cooling requirements while avoiding unnecessary energy consumption and excessive costs.

5. Parameter Optimization

Although traditional finite element methods have advantages in modeling physical mechanisms, they still face limitations in engineering applications, such as complex modeling processes and high requirements for mesh quality. To overcome these issues, this study introduces the Random Forest (RF) algorithm to construct a data-driven prediction and optimization model based on finite element data obtained under different parameter combinations. This approach enables rapid prediction for various parameters and facilitates the identification of the optimal parameter combination.

5.1. Subsection

The Random Forest (RF) model is a typical ensemble learning algorithm commonly used for regression tasks. By integrating multiple decision trees, it not only possesses strong generalization capability but also performs exceptionally well when handling high-dimensional data and complex nonlinear relationships [40,41]:

$$\begin{aligned} \hat{y} &= \frac{1}{T}\sum_{t=1}^{T} h_t(x) \\ h_t &= \text{BuildTree}\left(\mathcal{D}^{(t)}, D\right) \\ \mathcal{D}^{(t)} &\sim \text{Bootstrap}(\mathcal{D}, \lfloor r \cdot m \rfloor) \end{aligned} \tag{16}$$

where T is the number of decision trees, D is the maximum depth of decision trees, and r is the sample proportion.

In this study, considering the highly nonlinear mapping relationship between input and output variables, the number of decision trees was set to 100 after multiple rounds of parameter tuning to ensure model stability, convergence to an optimal solution, and effective suppression of overfitting. Meanwhile, the maximum depth of each tree was limited to 5 to balance model complexity and computational efficiency. During training, each tree was constructed using 80% of the samples to enhance model robustness. This design allows the model to capture complex feature relationships while maintaining relatively low computational cost. The overall framework is illustrated in Figure 16.

A predictive model was established using the gas–liquid pressure ratio and nozzle inclination angle as input features, with the cooling plate surface temperature as the output feature. During model training, the input and output data were standardized and normalized using Equation (17) to eliminate dimensional differences that could affect model convergence and prediction accuracy, thereby enhancing the model's stability and generalization capability.

$$\begin{aligned} X_{std} &= \frac{X-\mu}{\sigma} \\ Y_{\text{norm}} &= \frac{Y-Y_{\min}}{Y_{\max}-Y_{\min}} \end{aligned} \tag{17}$$

where X is the original input feature value, μ is the mean value of the academician feature, σ is the standard deviation of the original feature, X_{std} is the standardized feature value,

Y is the original output, Y_{min} is the minimum value of the output variable, Y_{max} is the maximum value of the output variable, and Y_{norm} is the normalized output value.

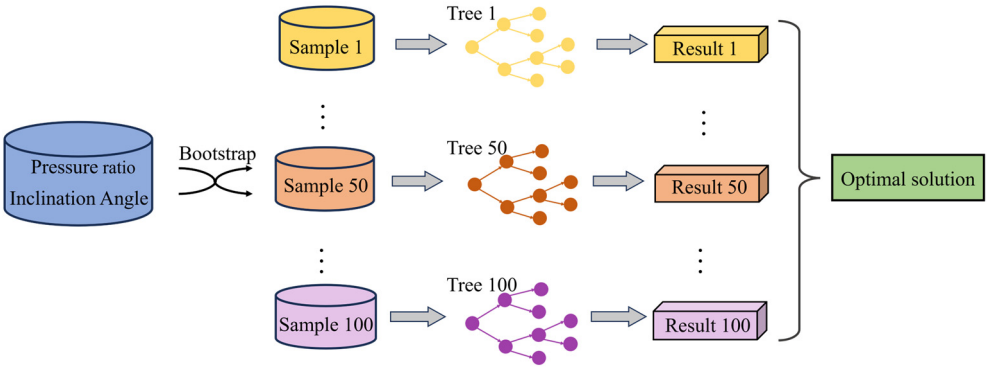


Figure 16. RF structure diagram.

Figure 17 shows the prediction results of the model on the training and testing sets. Overall, the RF model did not produce any significantly erroneous predictions across all datasets. Furthermore, the performance of the RF model on the training and testing sets was consistent, indicating no obvious overfitting.

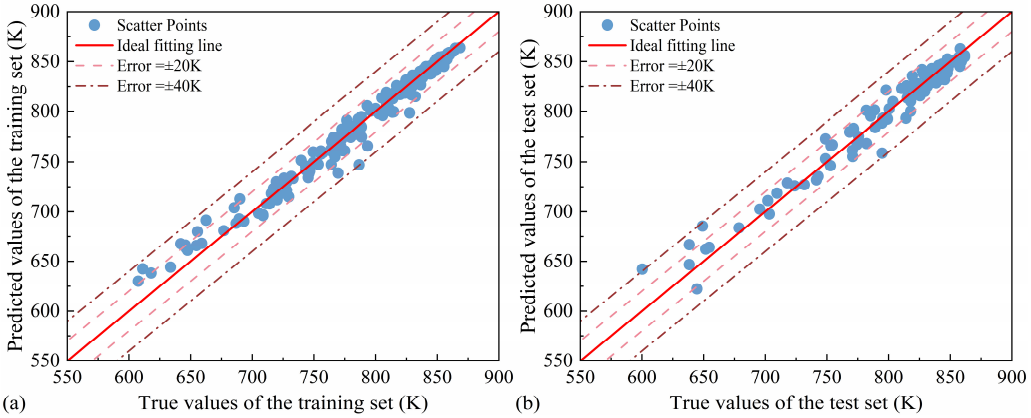


Figure 17. Variation curves of nozzle outlet momentum flux with (**a**) nozzle inclination angle and (**b**) gas–liquid pressure ratio.

To accurately evaluate the model's performance, the mean squared error (MSE), mean absolute error (MAE), and determination coefficient (R^2) were used as assessment metrics.

The formula of each evaluation index containing samples is shown as follows [42]:

Mean Square Error (MSE):

$$MSE = \frac{1}{n}\sum_{i=1}^{n}(y_i - \hat{y}_i)^2 \quad (18)$$

Mean absolute error (MAE):

$$MAE = \frac{1}{n}\sum_{i=1}^{n}|y_i - \hat{y}_i| \quad (19)$$

Determination coefficient (R^2):

$$R^2 = 1 - \frac{\sum(y_i - \hat{y}_i)^2}{\sum(\overline{y}_i - y_i)^2} \quad (20)$$

where y_i is the number of decision trees, $\hat{y}_i$ is the maximum depth of decision trees, and $\overline{y}_i$ is the sample proportion.

To further verify the reliability and high accuracy of the RF model in predicting the temperature field, the SVM model was selected as a reference for comparative analysis, and the corresponding performance metrics are summarized in Table 5. As shown in the table, the RF model outperforms the SVM model across all evaluation indicators and maintains a high level of consistency between the training and test sets, demonstrating strong fitting capability and robust generalization performance. In summary, the RF model exhibits superior overall performance in this study and can be considered a reliable approach for predicting and analyzing the surface temperature field of the cooling plate.

Table 5. Evaluation index of RF model.

Model	Training Set			Test Set		
	RMSE	**MAE**	**R^2**	**RMSE**	**MAE**	**R^2**
RF	8.447	5.411	0.979	11.645	8.249	0.968
SVM	17.219	11.192	0.801	18.504	13.178	0.779

5.2. PSO Optimizes RF Model

The Particle Swarm Optimization (PSO) algorithm, proposed by Eberhart and Kennedy in 1995, is a population-based global optimization method [43]. In this approach, each potential solution is represented as a particle, and all particles move within the search space. By dynamically adjusting their velocities and positions based on both their individual historical best positions and the global best position of the swarm, the particles gradually converge toward the optimal solution:

$$\begin{aligned} v_i^{sc} &= \omega \cdot v_i^{sc} + c_1 \text{ rand } (1) \cdot \left(\text{Pbest}^{sc} - x_i^{sc} \right) + c_2 \text{ rand } (2) \cdot \left(\text{Gbest}^{sc} - x_i^{sc} \right) \\ x_i^{sc} &= x_i^{sc} + 0.5 v_i^{sc} \end{aligned} \tag{21}$$

where ω is inertia weight, c_1 and c_2 are learning factors that determine the extent to which particles move toward the optimal position, and rand (1), rand (2) are random value function [44].

The PSO algorithm was combined with the RF model to optimize the gas–liquid pressure ratio and nozzle inclination angle. In this method, each parameter combination is cross-validated on the training set to evaluate the fitness of each particle. The particles then iteratively update their positions based on their individual historical best and the global best of the swarm, ultimately yielding the optimal parameter combination [45]. To implement this process, a corresponding multi-objective optimization function was constructed, and practical production constraints were incorporated into the optimization framework [46,47]:

$$\begin{aligned} &\min_{\alpha,\beta} \text{Loss } (\alpha, \beta) \\ &\text{s.t.} \begin{cases} 0 \le \alpha \le 3 \\ 0 \le \beta \le 90 \end{cases} \end{aligned} \tag{22}$$

Based on the overall optimization results, it can be concluded that using the PSO algorithm to determine the optimal geometric parameter combination is both feasible and effective. The obtained optimal parameter combination is presented in Table 6.

Table 6. Optimal parameter combination.

Parameter Variable	Gas–Liquid Pressure Ratio	Inclination Angle
Optimal solution	2.76	61.98°

As shown in Figure 18a, the algorithm exhibits a rapid convergence rate during the initial iterations and gradually stabilizes after approximately 49 iterations. Based on the geometric parameters optimized by the PSO-RF model, experiments were conducted to calculate the surface heat transfer coefficient along the path shown in Figure 15a, and the results are presented in Figure 18b. Compared with the original nozzle, the optimized geometric parameters effectively improve the jet coverage and impingement distribution, allowing the cooling medium to spread more uniformly across the surface of the cooling plate and enhance jet impingement in the edge regions, thereby strengthening local heat transfer. Meanwhile, the velocity distribution becomes more uniform, reducing the alternation between high- and low-speed regions, which in turn decreases fluctuations in the heat transfer coefficient and yields smoother peak transitions. These improvements significantly enhance cooling uniformity. Furthermore, the optimized nozzle achieves an average heat transfer coefficient of 13,877.86 W/m^2·K, representing a 55.57% increase compared with the original design, as shown in Table 7. Therefore, the optimized parameter combination demonstrates a substantial advantage in improving the cooling performance of the plate surface, achieving simultaneous enhancements in both cooling uniformity and efficiency.

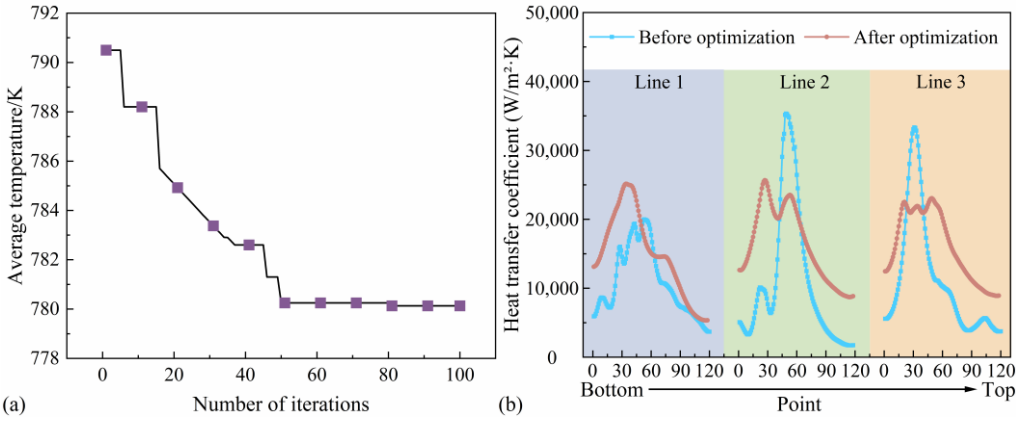


Figure 18. (**a**) Iterative result graph and (**b**) heat transfer coefficient under the optimal parameters.

Table 7. Comparison of Results Before and after Optimization.

	Gas–Liquid Pressure Ratio	Inclination Angle/°	Heat Transfer Coefficient/(W/m^2·K)
Before optimization	1.57	Circular	8919.51
After optimization	2.76	62	13,877.86

5.3. Water Spray Ring Experiment

To verify the practical effectiveness of the optimized nozzle, the spray ring was redesigned based on the optimized parameter combination, as shown in Figure 19a. The redesigned spray ring was then tested on the three-roll planetary elongation mill, and metallographic analyses of the rolled tubes were performed, as presented in Figure 19b,c. The results show that the intensified cooling provided by the new spray ring leads to significant grain refinement in the copper tubes. This is because the optimized nozzle structure increases the cooling coefficient and reduces the roll-surface temperature, thereby shortening the residence time of the tube in the high-temperature stage, promoting dynamic recrystallization, and suppressing grain growth [48,49]. Furthermore, grain refinement improves not only the microstructural uniformity but also the mechanical properties of the tubes, such as yield strength and ductility, while enhancing dimensional stability. Consequently, the overall product quality is improved, which is beneficial for the subsequent manufacturing of small-diameter tubes [50].



Figure 19. (**a**) Optimized spray ring, (**b**) microstructure of rolled copper tube before optimization, and (**c**) microstructure of rolled copper tube after optimization.

6. Conclusions

In this study, a deep integration of multi-physics coupled simulation and machine learning algorithms was employed to systematically investigate the effects of the elliptical nozzle's major axis inclination angle and gas–liquid pressure ratio on the surface temperature distribution and homogenization of high-temperature cooling plates. The results indicate that:

Compared with a circular nozzle of the same equivalent diameter, the elliptical nozzle effectively reduces flow resistance and energy loss, resulting in a higher jet exit velocity and momentum flux. In addition, the elliptical nozzle creates multiple continuously distributed local cooling centers on the target surface, which not only expands the cooling coverage area but also improves overall cooling uniformity.

The temperature field on the hot plate surface is highly sensitive to nozzle geometry and the gas–liquid pressure ratio. Compared with circular nozzles of the same equivalent diameter, elliptical nozzles exhibit superior cooling performance. The nozzle inclination angle significantly affects cooling uniformity by altering the flow direction and superposition behavior of the coolant. As the major-axis inclination angle of the elliptical nozzle increases, the surface heat transfer coefficient first rises and then decreases. Moreover, when the gas–liquid pressure ratio is 1, the addition of nitrogen has little effect on increasing the coolant velocity; however, as the ratio continues to increase, its velocity-enhancing effect becomes increasingly pronounced.

Using the PSO algorithm in combination with the RF model for parameter optimization, the heat transfer coefficient reaches 13,877.86 $W/m^2 \cdot K$ at a gas–liquid pressure ratio of 2.76 and an elliptical nozzle major-axis inclination angle of 62°, representing a 55.57% improvement compared with the parameters currently used in practice.

Metallographic experiments conducted with the optimized spray ring show that the grain structure of the rolled copper tube becomes significantly refined and the roll surface temperature is effectively reduced, confirming the effectiveness of the proposed optimization scheme.

Author Contributions: Conceptualization, Y.J.; methodology, Y.S. and H.S.; software, Y.S. and J.L.; validation, Y.S. and Y.J.; formal analysis, F.Y.; investigation, F.Y., H.S. and D.C.; resources, H.S. and H.C.; data curation, F.Y. and Y.S.; writing—original draft preparation, Y.S.; writing—review and editing, H.S. and D.C.; visualization, Y.S. and J.L.; supervision, H.C.; project administration, D.C.; funding acquisition, J.L. All authors have read and agreed to the published version of the manuscript.

Funding: This research was funded by the Basic Research Projects of Liaoning Provincial Department of Education (LJ212510144021).

Data Availability Statement: Data are contained within the article.

Acknowledgments: The authors would also like to thank Zhuo Sha for his valuable comments.

Conflicts of Interest: The authors declare no conflicts of interest.

References

1. Yin, Z.W. Three-Roll Planetary Rolling Mill Motion Analysis and Test Research. *Adv. Mater. Res.* **2013**, *712*, 1724–1728. [CrossRef]
2. Shih, C.K.; Hung, C. Experimental and numerical analyses on three-roll planetary rolling process. *J. Mater. Process. Technol.* **2003**, *142*, 702–709. [CrossRef]
3. Han, Y.; Zhang, X.B.; Wang, Z.X.; Xiao, Y.; Gao, X.-L.; Zhao, Y.-Q. Study on cooling process of copper tube after three-roll planetary rolling. *Int. Commun. Heat Mass Transf.* **2020**, *110*, 104393. [CrossRef]
4. Li, B.; Zhang, S.H.; Zhang, G.L.; Zhang, H.Y.; Zhang, H.Q. Microstructure simulation of copper tube and its application in three roll planetary rolling. *Mater. Sci. Technol.* **2007**, *23*, 715–722. [CrossRef]
5. Li, B.; Zhang, S.H.; Zhang, H.Q.; Zhang, G.L. Microstructure and properties of copper tube during three-roll planetary rolling. *J. Mater. Eng. Perform.* **2008**, *17*, 499–505. [CrossRef]
6. Li, M.-M.; Yang, B.; Zhao, H.-J. "Black stripe" Defect of Copper Tubes Result from Planetary Rolling-draw. *Nonferrous Met. Sci. Eng.* **2011**, *2*, 36–39.
7. Li, B.; Zhang, S.H.; Zhang, G.L.; Zhang, H.Q. Prediction of 3-D temperature field of TP2 copper tubes in three-roll planetary rolling process. *J. Mater. Process. Tech.* **2007**, *205*, 370–375. [CrossRef]
8. Luo, C.; Keife, H. Friction in three-roll planetary tube rolling process. *Met Form* **2008**, *1*, 447–452.
9. Li, L.M.; Zang, Y.; Zhang, Z.Z.; Yao, H.Z.; Zhang, B. The effect of friction state on the planetary rolling process of copper tube. *J. Plast. Eng.* **2009**, *16*, 115–119.
10. Xiao, Y.; Cheng, Y.; Shen, M.; Yao, P.; Du, J.; Ji, D.; Zhao, H.; Liu, S.; Hua, L. Friction and wear behavior of copper metal matrix composites at temperatures up to 800 C. *J. Mater. Res. Technol.* **2022**, *19*, 2050–2062. [CrossRef]
11. Kim, K.C.; Park, I.J.; Ryu, H.J.; Lee, S. Correlation of Microstructure and Thermal-Fatigue Properties of Centrifugally Cast High-Speed Steel Rolls. *Metall. Mater. Trans. A* **2004**, *35*, 481–492. [CrossRef]
12. Lee, S.; Kim, H.D.; Ryu, H.J.; Shin, K. Correlation of Microstructure and Thermal Fatigue Property of Three Work Rolls. *Metall. Mater. Trans. A* **1997**, *28*, 2595–2608. [CrossRef]
13. Bapu, R. Experimental analysis of heat transfer and multi objective optimization of swirling jet impingement on a flat surface. *J. Appl. Fluid Mech.* **2019**, *12*, 803–817. [CrossRef]
14. Uddin, N.; Kee, P.T.W.; Weigand, B. Heat transfer by jet impingement: A review of heat transfer correlations and high-fidelity simulations. *Appl. Therm. Eng.* **2024**, *257*, 124258. [CrossRef]
15. Zuckerman, N.; Lior, N. Jet impingement heat transfer: Physics, correlations, and numerical modeling. *Adv. Heat Transf.* **2006**, *39*, 565–631.
16. Cademartori, S.; Cravero, C.; Marini, M.; Marsano, D. CFD simulation of the slot jet impingement heat transfer process and application to a temperature control system for galvanizing line of metal band. *Appl. Sci.* **2021**, *11*, 1149. [CrossRef]
17. Manca, O.; Mesolella, P.; Nardini, S.; Ricci, D. Numerical study of a confined slot impinging jet with nanofluids. *Nanoscale Res. Lett.* **2011**, *6*, 188. [CrossRef] [PubMed]
18. Du, X.; Yang, Z.; Jin, Z.; Xia, C.; Bao, D. A comparative study of passive control on flow structure evolution and convective heat transfer enhancement for impinging jet. *Int. J. Heat Mass Transf.* **2018**, *126*, 256–280. [CrossRef]
19. Joshi, J.; Sahu, S.K. Effect of nozzle configurations and jet orientations on thermal performance of jet impingement on convex surface. *Int. J. Therm. Sci.* **2024**, *203*, 109171. [CrossRef]
20. Joshi, J.; Sahu, S.K. Analyze the influence of nozzle shape and orientation on inline arrangement of multiple jets impingement on a concave surface. *Exp. Heat Transf.* **2024**, *38*, 519–539. [CrossRef]
21. Teramoto, H.; Kiwata, T.; Yajima, K. Influence of nozzle aspect ratio and orientation on flow characteristics of multiple elliptic jets. *J. Fluid Sci. Technol.* **2020**, *15*, JFST0012. [CrossRef]
22. Schuller, T.; Jalaal, M.; Fanzio, P.; Galindo-Rosales, F.J. Optimal shape design of printing nozzles for extrusion-based additive manufacturing. *Addit. Manuf.* **2024**, *84*, 104130. [CrossRef]
23. Yang, X.; Xi, T.; Qin, Y.; Zhang, H.; Wang, Y. Computational fluid dynamics–Discrete phase method simulations in process engineering: A review of recent progress. *Appl. Sci.* **2024**, *14*, 3856. [CrossRef]
24. Wu, Y.; Liu, D.; Hu, J.; Ma, J.; Chen, X. Comparative study of two fluid model and dense discrete phase model for simulations of gas–solid hydrodynamics in circulating fluidized beds. *Particuology* **2021**, *55*, 108–117. [CrossRef]
25. Yang, Z.X.; Du, Y.C.; Liu, J.Y.; Tang, Y.; Dong, X.L.; Huang, A.C. High-Pressure Fine Water Mist Nozzle Retrofit Experiment and Numerical Simulation Study. *Processes* **2025**, *13*, 642. [CrossRef]

26. Huang, W.; He, X.; Liu, C.; Li, X.; Liu, Y.; Collier, C.P.; Srijanto, B.R.; Liu, J.; Cheng, J. Droplet evaporation on hot micro-structured superhydrophobic surfaces: Analysis of evaporation from droplet cap and base surfaces. *Int. J. Heat Mass Transf.* **2022**, *185*, 122314. [CrossRef]
27. Sidebotham, G.; Sidebotham, G. Evaporation and mass transfer fundamentals. In *Heat Transfer Modeling: An Inductive Approach*; Springer: Cham, Switzerland, 2015; pp. 475–516.
28. Reyjal, M.; Tavares, J.R.; Virgilio, N.; Fradette, L. Is the Maxwell–Garnett continuum model valid to predict the thermal conductivity of particle-stabilized (Pickering) emulsions? *Ind. Eng. Chem. Res.* **2013**, *52*, 4962–4966. [CrossRef]
29. Bian, G.; Cheng, M.; Liu, Y.; Zhang, S.-H. Wear Behaviors of GH4169 Super Alloy and 3Cr2W8V Tool Steel Under Dry Rolling Condition. *Acta Metall. Sin. (Engl. Lett.)* **2018**, *31*, 983–996. [CrossRef]
30. González, J.; Meana-Fernández, A.; Pérez, I.V.; Oro, J.M.F. Minor Loss Coefficient for Abrupt Section Changes in a Cylindrical Pipe Using a Numerical Approach. *Fluids* **2024**, *9*, 152. [CrossRef]
31. Lee, S.J.; Kim, J.Y.; Hong, J.G. Asymmetric spray characteristics according to Y-jet nozzle orifice shape and spray conditions. *ACS Omega* **2023**, *8*, 14490–14498. [CrossRef]
32. Xu, Y.; Fan, D.; Wang, L. Vortex–wall interactions in elliptic impinging synthetic jets. *Phys. Fluids* **2024**, *36*, 067139. [CrossRef]
33. Karbasi, M.; Jamei, M.; Ahmadianfar, I.; Asadi, A. Toward the accurate estimation of elliptical side orifice discharge coefficient applying two rigorous kernel-based data-intelligence paradigms. *Sci. Rep.* **2021**, *11*, 19784. [CrossRef]
34. Singh, G.K.; Pradhan, S.; Tanna, V. Experimental studies of two phase flow characteristics and void fraction predictions in steady state horizontal two-phase nitrogen flow. *Cryogenics* **2019**, *100*, 77–84. [CrossRef]
35. Nejatipour, P.; Khorsandi, B. Effect of nozzle geometry on the dynamics and mixing of self-similar turbulent jets. *Water Sci. Technol.* **2021**, *84*, 3907–3915. [CrossRef]
36. Qu, X.; Sui, H.; Liu, Y.; Zhang, Y.; Qi, X. An experimental study on two-phase characteristics of vertical injection of gas through a slot nozzle into a liquid bath. *Exp. Therm. Fluid Sci.* **2021**, *120*, 110222. [CrossRef]
37. Bandaru, S.V.R.; Villanueva, W.; Thakre, S.; Bechta, S. Multi-nozzle spray cooling of a reactor pressure vessel steel plate for the application of ex-vessel cooling. *Nucl. Eng. Des.* **2021**, *375*, 111101. [CrossRef]
38. Barbosa, F.V.; Teixeira, S.F.C.F.; Teixeira, J.C.F. Experimental and numerical study of multiple jets impinging a step surface. *Energies* **2021**, *14*, 6659. [CrossRef]
39. Babji, G.; Pujari, A.K. Flow and heat transfer studies of multijet impingement cooling for different configurations: A review. *Heat Transf.* **2023**, *52*, 1604–1672. [CrossRef]
40. Xiao, Z.; Fan, C.; Yuan, J.; Xu, X.; Gang, W. Comparison between artificial neural network and random forest for effective disaggregation of building cooling load. *Case Stud. Therm. Eng.* **2021**, *28*, 101589. [CrossRef]
41. Liu, G. Tropical climate prediction method combining random forest and feature fusion. *Int. J. Low-Carbon Technol.* **2025**, *20*, 154–166. [CrossRef]
42. Yue, F.; Shao, Y.; Sun, H.; Liu, J.; Chen, D.; Sha, Z. Multi-Field Coupling-and Data-Driven-Based Optimization of Cooling Process Parameters for Planetary Rolling Rolls. *Materials* **2025**, *18*, 4111. [CrossRef]
43. Yue, F.; Sha, Z.; Sun, H.; Chen, D.; Liu, J. Research on the Optimization of TP2 Copper Tube Drawing Process Parameters Based on Particle Swarm Algorithm and Radial Basis Neural Network. *Appl. Sci.* **2024**, *14*, 11203. [CrossRef]
44. Ambuj Machavaram, R. Optimizing energy expenditure in agricultural autonomous ground vehicles through a GPU-accelerated particle swarm optimization-artificial neural network framework. *Clean. Energy Syst.* **2024**, *9*, 100130. [CrossRef]
45. Sun, H.; Zhang, H.; Li, X.; Yuan, H. Modeling and Optimization of Parallel Vibration Reduction for Multi-Stage Mistuned Bladed Disk Systems in Aeroengines. *Aerosp. Sci. Technol.* **2025**, *168*, 111078. [CrossRef]
46. Ye, X.; Zhang, X.; Chen, Y.; Wei, Y.; Ding, Y. Prediction of maximum upward displacement of shield tunnel linings during construction using particle swarm optimization-random forest algorithm. *J. Zhejiang Univ.-Sci. A* **2024**, *25*, 1–17. [CrossRef]
47. Zheng, Y.; Zhang, H.; Zheng, G.; Hong, Y.; Wei, Z.; Sun, P. Research on Motion Transfer Method from Human Arm to Bionic Robot Arm Based on PSO-RF Algorithm. *Biomimetics* **2025**, *10*, 392. [CrossRef]
48. Saha, J.K.; Kundu, S.; Chandra, S.; Sinha, S.K.; Singhal, U.; Das, A.K. Mathematical modelling of roll cooling and roll surface stress. *ISIJ Int.* **2005**, *45*, 1641–1650. [CrossRef]
49. Seetharam, R.; Kanmani Subbu, S.; Davidson, M.J. Microstructure modeling of dynamically recrystallized grain size of sintered Al–4 wt% B4C composite during hot upsetting. *J. Eng. Mater. Technol.* **2018**, *140*, 021003. [CrossRef]
50. Hou, Y.; Mi, X.; Xie, H.; Zhang, W.; Huang, G.; Peng, L.; Feng, X.; Yang, Z. Size effect on mechanical properties and deformation behavior of pure copper wires considering free surface grains. *Materials* **2020**, *13*, 4563. [CrossRef]

Disclaimer/Publisher's Note: The statements, opinions and data contained in all publications are solely those of the individual author(s) and contributor(s) and not of MDPI and/or the editor(s). MDPI and/or the editor(s) disclaim responsibility for any injury to people or property resulting from any ideas, methods, instructions or products referred to in the content.